MOX-Report No. 19/2020

Integration of maps of activation times in computational cardiac electrophysiology

Stella, S.; Vergara, C.; Maines, M.; Catanzariti, D.; Africa, P.;

Dematté, C.; Centonze, M.; Nobile, F.; Del Greco, M.;

Quarteroni, A.

MOX, Dipartimento di Matematica
Politecnico di Milano, Via Bonardi 9 - 20133 Milano (Italy)

mox-dmat@polimi.it http://mox.polimi.it

Integration of maps of activation times in computational cardiac electrophysiology

Simone Stella[1], Christian Vergara[2], Massimiliano Maines[3], Domenico Catanzariti[3], Pasquale Claudio Africa[1], Cristina Demattè[3], Maurizio Centonze[4], Fabio Nobile[5], Maurizio Del Greco[3], Alfio Quarteroni[1,6]

March 12, 2020

[1] MOX, Dipartimento di Matematica, Politecnico di Milano, Milan, Italy
[2] LABS, Dipartimento di Chimica, Materiali e Ingegneria Chimica "Giulio Natta", Politecnico di Milano, Milan, Italy
[3] Divisione di Cardiologia, Ospedale S. Maria del Carmine, Rovereto (TN), Italy
[4] U.O. di Radiologia di Borgo-Pergine, Ospedale di Borgo Valsugana, Borgo Valsugana (TN), Italy
[5] CSQI, Institute of Mathematics, École Polytechnique Fédérale de Lausanne, Switzerland
[6] Institute of Mathematics, École Polytechnique Fédérale de Lausanne, Switzerland (professor emeritus)

Keywords: Cardiac electro-physiology, monodomain equation, Bueno-Orovio ionic model, activation times, Ensite NavX system, Cardiac Resynchronization Therapy

Abstract

In this work we used the monodomain equation in combination with the Bueno-Orovio ionic model for the prediction of the activation times in cardiac electro-physiology. We considered four patients who suffered from Left Bundle Branch Block (LBBB) and patient-specific maps of activation times obtained by inserting in the ventricles electrodes located on catheters. We used activation maps acquired at the septum as input data for the model and maps at the epicardial veins for the validation of the monodomain model in the context of a normal excitation. In particular, a first set (half) of the latter were used to estimate the conductivities of the patient and a second set (the remaining half) to compute the errors of the numerical simulations. We found an excellent agreement between measures and numerical results. Our validated computational tool could be used to accurately predict activation times at the epicardial veins, allowing to shorten the mapping procedure and reduce the exposition to radiations. This could be of great interest for clinical applications, for example in the *Cardiac*

Resynchronization Therapy (CRT) where such mapping is commonly used to determine the best point of stimulus.

1 Introduction

Electrophysiology is a fundamental research field in applied mathematics since Hodgkin and Huxley described for the first time the propagation of action potentials in cells [3]. Mathematical and numerical modeling in cardiac electrophysiology in the last decades have assumed a key role to better understand cardiac muscle function and to study how several cardiac diseases develop and to provide concrete answers to clinical problems. Challenging issues consist of selecting accurate and efficient numerical methods for the approximate solution of such models and in their parameter estimation to fit patient-specific data.

To describe the propagation of the electrical signal in the heart muscle two mathematical approaches are available: the bidomain and the monodomain models [30, 29]. The former is the result of the application of conservation of charge together with constitutive models. It describes the propagation of the trans-membrane potential and compute both the internal and external cell potentials. The monodomain model is a simplification of the bidomain one, assuming that the external and internal conductivity tensors are proportional. Both models have to be coupled with a ionic model, a system of ODEs which describes the evolution of the trans-membrane potential in a single cell by means of suitable gating variables.

Validation of these mathematical models is fundamental to provide clinicians a reliable tool to study and predict the cardiac function accurately.

A first attempt in this direction consisted of comparing numerical results (obtained either by the bidomain or monodomain model) with measures of electrical activity obtained by optical imaging during *ex-vivo* experiments on animal hearts. In particular, qualitative comparisons have been provided in [4, 26, 38] for action potentials and in [35, 10] for activation times. Other works instead quantified the discrepancy between results ans measures; in particular in [1] the authors focused on the action potential at a selected point, whereas in [17, 24] on activation times at several epicardial points.

A second set of results focused on human ideal geometries, proposing benchmark simulation protocols to be validated against gold-standard activation times obtained from experimental measures. In particular, [40] considered a slab of tissue, whereas [41] an idealized left ventricle.

A third group of studies addressed qualitative comparisons in real human geometries. In particular, in [20] the authors compared the phase distribution during ventricular fibrillation with some reference electrical data, whereas in [8] they studied the reliability of ECG obtained with an electro-mechanical simulation.

We finally mention [7, 42] where a quantitative comparison between in-vivo

measures of activation times and those provided by the Eikonal equation in the presence of a personalized Purkinje network was carried out.

However, a quantitative comparison of the cardiac electrical activity obtained with monodomain or bidomain models on real human geometries against clinical measures acquired in vivo is still missing. One reason is that patient-specific electrical data are very difficult to obtain, since they are based on invasive clinical procedures and acquired only when strictly necessary for the clinical practice.

Our work aims at proposing a new approach for validating the monodomain model in the context of the electric propagation in the human left ventricle using patient-specific activation maps. In particular, we only consider normal excitation with sinus rhythm, and not, e.g., tachicardia and fibrillation. For each patient we had at disposal activation times at some points located at the septum and at the epicardial veins. The first dataset was used to provide an input for the numerical simulation, whereas the second one was split into two subgroups, the first one used to estimate the conductivities of the patient and the second one to validate the accuracy of the numerical solution.

More specifically, we present the mathematical and numerical model in Section 2. The whole pipeline of data acquisition and elaboration is reported in Section 3, whereas the numerical results are presented and discussed in Section 4. Finally, in Section 5, we provide conclusions and discuss possible future developments.

2 Mathematical and numerical model

In this section we present the mathematical model for cardiac electrophysiology, *i.e.* the monodomain model, and the corresponding numerical methods considered in this work. The choice of the monodomain model has been motivated by its lower computational cost, yet providing comparable accuracy with respect to the bidomain model, at least in the cases of physiological propagations [26].

Referring to Figure 1, the cardiac tissue conductivity is modeled as a tensor $\mathbb{D}$ defined as

$$\mathbb{D} = \sigma_s \nVdash + (\sigma_f - \sigma_s)\boldsymbol{f} \otimes \boldsymbol{f} + (\sigma_n - \sigma_s)\boldsymbol{n} \otimes \boldsymbol{n}, \tag{1}$$

where σ_f, σ_n and σ_s are the conductivities along the fibers direction $\boldsymbol{f}$, the normal direction $\boldsymbol{n}$ and the transversal direction $\boldsymbol{s}$ (orthogonal to the sheets plane $\boldsymbol{f}$-$\boldsymbol{n}$), respectively, to be determined in order to fit the patient-specific activation times.

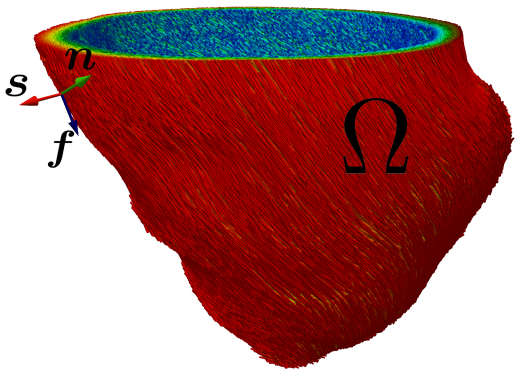

Figure 1: Computational domain.

Assuming an external applied stimulus I_{app}, as provided in our case by activation time measures located at the septum, the monodomain model in the computational domain Ω and over a time interval $(0, T]$ reads [31, 34]:

Find, for each t, the electrical potential $u : \Omega \to \mathbb{R}$ and the gating variables $\boldsymbol{w} : \Omega \to \mathbb{R}^3$, such that

$$\chi C_m \frac{\partial u}{\partial t} - \nabla \cdot (\mathbb{D}\nabla u) + \chi I_{\text{ion}}(u, \boldsymbol{w}) = I_{\text{app}} \qquad \text{in } \Omega, \tag{2a}$$

$$\frac{d\boldsymbol{w}}{dt} = \boldsymbol{R}(u, \boldsymbol{w}) \qquad \text{in } \Omega, \tag{2b}$$

where the ionic current $I_{\text{ion}}(u, \boldsymbol{w})$ and $\boldsymbol{R} \in \mathbb{R}^3$ are chosen according to the Bueno-Orovio ionic model [2]. In particular, $I_{\text{ion}} = I_{\text{ion},1} + I_{\text{ion},2} + I_{\text{ion},3}$, with

$$I_{\text{ion},1} = -\frac{H(u - V_1)(u - V_1)(\widetilde{V} - u)w_1}{\tau_1},$$

$$I_{\text{ion},2} = \frac{1 - H(u - V_2)(u - V_o)}{H(u - V_o)(\tau_{o2} - \tau_{o1}) + \tau_{o1}} + \frac{H(u - V_2)}{H(u - V_2)(\tau_{22} - \tau_{21}) + \tau_{21}},$$

$$I_{\text{ion},3} = -\frac{H(u - V_2)}{\tau_3} w_2 w_3,$$

for suitable constants V_o, V_1, V_2, $\widetilde{V}$, τ_1, τ_3, τ_{o1}, τ_{o2}, τ_{21}, τ_{22} and where H is the Heaviside function. Moreover, χ is the surface area-to-volume ratio and C_m the trans-membrane capacitance. System (2) has been equipped with suitable initial conditions for u and $\boldsymbol{w}$ and homogeneous Neumann conditions on $\partial\Omega$ for u.

The time discretization we used to numerically approximate system (2) relies at each time step $t^{n+1} = (n+1)\Delta t$ first on a forward Euler method for equation (2b), *i.e.*

$$\frac{\boldsymbol{w}^{n+1} - \boldsymbol{w}^n}{\Delta t} = \boldsymbol{R}(u^n, \boldsymbol{w}^n) \qquad \text{in } \Omega, \tag{4}$$

Δt being the time step length, and then on a first order semi-implicit method for (2a), i.e.

$$\chi C_{\mathrm{m}} \frac{u^{n+1}-u^n}{\Delta t} - \nabla\cdot\left(\mathbb{D}\nabla u^{n+1}\right) + \chi\left(I_{\mathrm{ion},1}^{n+1} + I_{\mathrm{ion},2}^{n+1} + I_{\mathrm{ion},3}^{n+1}\right) = I_{\mathrm{app}}(t^{n+1}) \qquad \text{in } \Omega, \tag{5}$$

with

$$\begin{aligned} I_{\mathrm{ion},1}^{n+1} &= -\frac{H(u^n - V_1)(u^{n+1} - V_1)(\widetilde{V} - u^n)w_1^{n+1}}{\tau_1}, \\ I_{\mathrm{ion},2}^{n+1} &= \frac{1 - H(u^n - V_2)(u^{n+1} - V_o)}{H(u^n - V_o)(\tau_{o2} - \tau_{o1}) + \tau_{o1}} + \frac{H(u^n - V_2)}{H(u^n - V_2)(\tau_{22} - \tau_{21}) + \tau_{21}}, \\ I_{\mathrm{ion},3}^{n+1} &= -\frac{H(u^n - V_2)}{\tau_3} w_2^{n+1} w_3^{n+1}, \end{aligned} \tag{6}$$

where the diffusion term has been treated implicitly and the non-linear terms have been linearized, see also [33]. In particular, at each time we first updated $\boldsymbol{w}^{n+1}$ for a given u^n by means of (4), then we solved (5) and (6) by using the up-to-date gating variables. Such time discretization lead to a conditionally stable method with a bound on time step Δt which is independent of the mesh size and which is milder with respect to the Δt required to reach the desired accuracy [27, 31].

As for the space discretization, we used continuous Finite Elements of order 1 on hexahedral meshes. The stiffness and the mass matrices were both approximated consistently, *i.e.* without lumping the resulting matrices. The ionic current term I_{ion} has been discretized using the Ionic Current Interpolation (ICI) method [39]: first I_{ion} has been computed using the values of u and $\boldsymbol{w}$ at the degrees of freedom, then it has been interpolated at quadrature nodes. Such approach is relatively inexpensive and less memory-demanding than solving the ODE system and computing I_{ion} directly at quadrature nodes (SVI), while the numerical accuracy is not affected at the small mesh size required to capture the propagating front. The resulting linear system arising at each time step has been solved by the GMRES method [44] preconditioned with the Jacobi preconditioner.

Finally, we highlight the importance of including cardiac fibers in electrophysiology models, since electrical propagation occurs in a different way along the fibers and orthogonally to them. However, standard imaging techniques do not provide geometric information on the fibers, whose dimension is typically smaller than the spatial resolution. For this reason, the fiber orientation over the myocardial tissue has been here determined using the Laplace-Dirichlet rule-based algorithm described in [18].

3 Processing of geometric and electrical data

In this section we illustrate the strategies used for data processing. In particular, in Section 3.1 we detail the geometric reconstruction, whereas in Section 3.2 the activation time maps and their integration with geometric data. Finally, in Section 3.3 we set the inverse problem used to provide the integration of electrical data into the numerical experiments and the estimation of the conductivities for a validation of the monodomain model in the context of a normal excitation. All the medical data, both geometric and electrical, have been provided by Ospedale S. Maria del Carmine, Rovereto (TN), Italy.

3.1 Imaging data acquisition and geometric reconstruction

In this study four patients have been considered, from now on referred to as P1, P2, P3, and P4, who underwent a non-contrast enhanced cardiac and respiratory gated 3D MRI acquisition of both ventricles. Image sequences were performed with a 1.5-Tesla MRI Unit (Magnetom Aera, Siemens Medical Systems, Erlangen, Germany). The following parameters have been used: pixel resolution $2.34 \times 2.34\ mm^2$; TE (echo time) $0.99\ ms$; TR (repetition time) $724\ ms$; slice thickness $8\ mm$ with 14 slices; acquisition matrix 192×144; flip angle 40^o.

We performed a semi-automatic segmentation of the two ventricle geometries by using the free open-source software `MITK` [28], which allowed us to segment each MRI slice and to interpolate the ventricle surface between slices. The first step consisted of capping the two surfaces at the base of the ventricle, then to connect them with a triangulated base using the approach reported in [25]. Once two closed triangulated surfaces of both epicardium and endocardium of the left ventricle were obtained, a surface mesh was generated by means of a set of new meshing tools [25] developed as an extension to the `VMTK` software [22]. A remeshing procedure on the whole closed surface was then performed in order to prescribe a target mesh size. Finally, a volumetric hexahedral mesh of the left ventricle was generated. In Figure 2 the four patient-specific reconstructed volumes of the left ventricles with the generated muscle fibers are displayed.

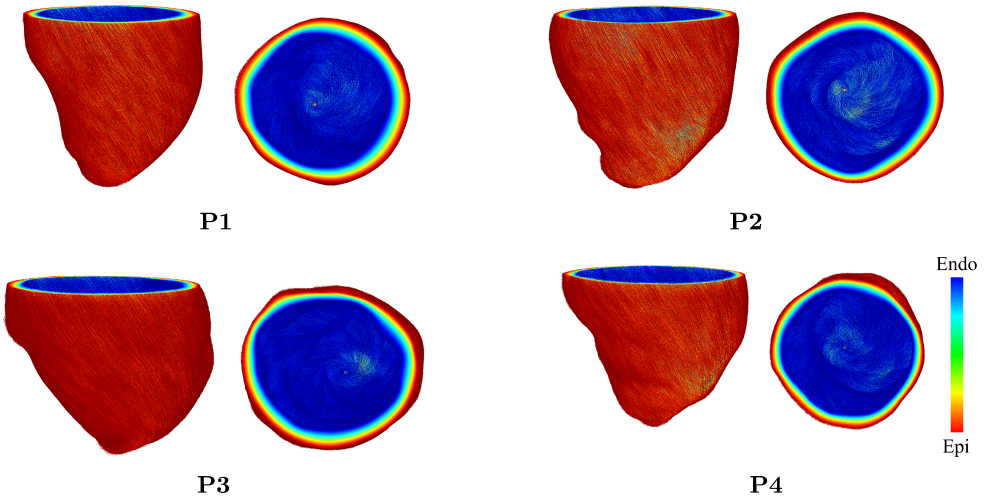

Figure 2: Patient-specific reconstructed geometries. For each case: on the left the frontal view, on the right base view. The generated muscle fibers are also reported.

3.2 Activation maps acquisition

A mapping of the septal surface located in the right ventricle and of the coronary veins located at the epicardium of the left ventricle has been performed (some days after the MRI acquisition) for all the four subjects through the use of the Ensite NavX system [5] to record local activation times (referred to also as electrical data). The latter represents, for each point of acquisition, the time difference between two instants, one measured on an extracardiac reference electrode and another one representing the steepest negative intrinsic deflection in the electrogram recorded on an intracardiac electrode and indicating that the activation wavefront has reached the point under investigation. The Ensite NavX system allows to perform an accurate real-time three dimensional catheter navigation to obtain maps of activation times. For this study, a 5 Fr steerable 10-pole catheter has been inserted through the left subclavian vein. The four subjects considered in the present study were affected by a Left Bundle Branch Block (LBBB), a cardiac conduction abnormality due to an interruption of the His bundle which causes a delayed activation of the left ventricle, and all the Ensite NavX acquisitions were made for clinical purposes.

We subdivided the electrical data at disposal into three subsets, each of them composed by the activation times and the coordinates of the corresponding points:

- *Septal data*: acquired at the septum and used here to provide the input current I_{app} in (5);
- *epicardial veins data, group I*: corresponds to half of the epicardial vein

measures we have at disposal, in particular it is composed by the points with the earliest activation times. This set is used to calibrate the conductivities of the patient;

- *epicardial veins data, group II*: corresponds to the remaining half of epicardial vein measures, in particular it is composed by the points with the highest activation times. In the spirit of a cross-validation, this set has been used to compute the discrepancies with the numerical solution and thus provide a validation of the latter.

In Table 1 we report the number of activation time measurements N^S (septal), N_I^V (epicardial vein, group I) and N_{II}^V (epicardial vein, group II) used in this work for each patient.

	P1	P2	P3	P4
N^S	132	15	9	4
N_I^V	8	26	19	16
N_{II}^V	8	26	18	15

Table 1: Total number of measurements acquired at the septum and at the epicardial veins for each patient.

In order to include in our simulation framework measured activation maps obtained from Ensite NavX (electrical data) onto the reconstructed geometries obtained from MRI (geometric data), we needed to merge geometric and electrical data. Since the MRI units and the Ensite NavX are two distinct systems collecting clinical data, the reconstructed patient-specific geometry and the corresponding activation map point cloud were linked to two distinct reference systems.

In order to make them compatible, we applied to each patient the following procedure based on the following three steps:

- **Reference points selection**: we selected three points for each set of data (geometric and electrical) as a reference. Two of them have been chosen on the coronary sinus, the third one on the septal surface of the right ventricle (see Figure 3, left block). We then verified, owing to the clinicians experience, that the two points of each couple in fact corresponded to the same physical point;

- **Geometric alignment**: we applied a rotation and translation to the point cloud of electrical data so that the three couples of reference points identified at the previous step coincided (see Figure 3, middle block). In fact, this guaranteed that the point cloud of electrical data lay as much as possible in correspondence of the geometric MRI data;

- **Nearest Neighbor Search (NNS) projection**: as a consequence of the geometric discrepancy still present between the two sets of data (geometric and electrical ones) due to the different instants acquisitions of MRI and Ensite NavX, we applied for the point cloud of electrical data the Euclidean NNS procedure [21]. This allowed us to select for each point of the cloud the nearest one among the geometric data belonging to the external (epicardial or septal) surface of the left ventricle. We finally moved each cloud point accordingly, so that it coincided with the geometric nearest one determined at the previous step (see Figure 3, right block).

This procedure, depicted in Figure 3, has been implemented in a Python script interacting with the Paraview software (Reference points selection and geometric alignment) and in MATLAB (NNS projection).

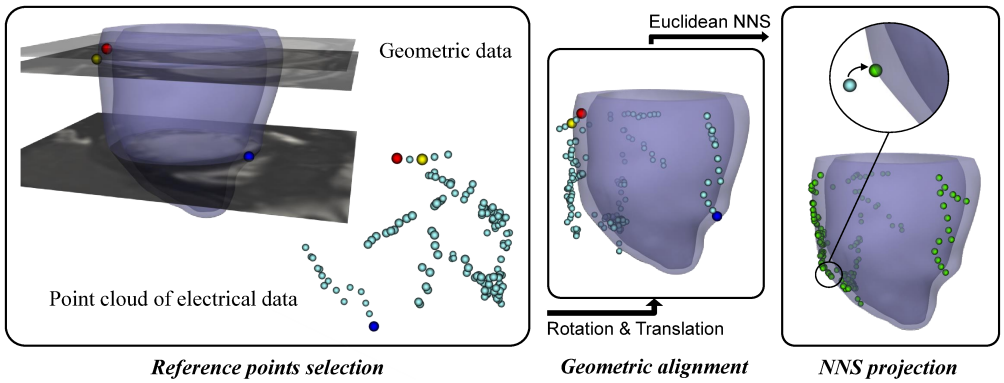

Figure 3: Graphical representation of the procedure for alignment of electrical and geometric data.

At the end of the alignment procedure we could identify

- the septal data $(\boldsymbol{x}_1^S, \tau_1^S), \ldots, (\boldsymbol{x}_j^S, \tau_j^S), \ldots, (\boldsymbol{x}_{N^S}^S, \tau_{N^S}^S)$;
- the epicardial veins data belonging to group I $(\boldsymbol{x}_1^{V-I}, \tau_1^{V-I}), \ldots, (\boldsymbol{x}_j^{V-I}, \tau_j^{V-I}), \ldots, (\boldsymbol{x}_{N_I^V}^{V-I}, \tau_{N_I^V}^{V-I})$;
- the epicardial veins data belonging to group II $(\boldsymbol{x}_1^{V-II}, \tau_1^{V-II}), \ldots, (\boldsymbol{x}_j^{V-II}, \tau_j^{V-II}), \ldots, (\boldsymbol{x}_{N_{II}^V}^{V-II}, \tau_{N_{II}^V}^{V-II})$.

In Figure 4, we report the final results of the alignment procedure for all the four patients with the corresponding patient-specific activation time measurements.

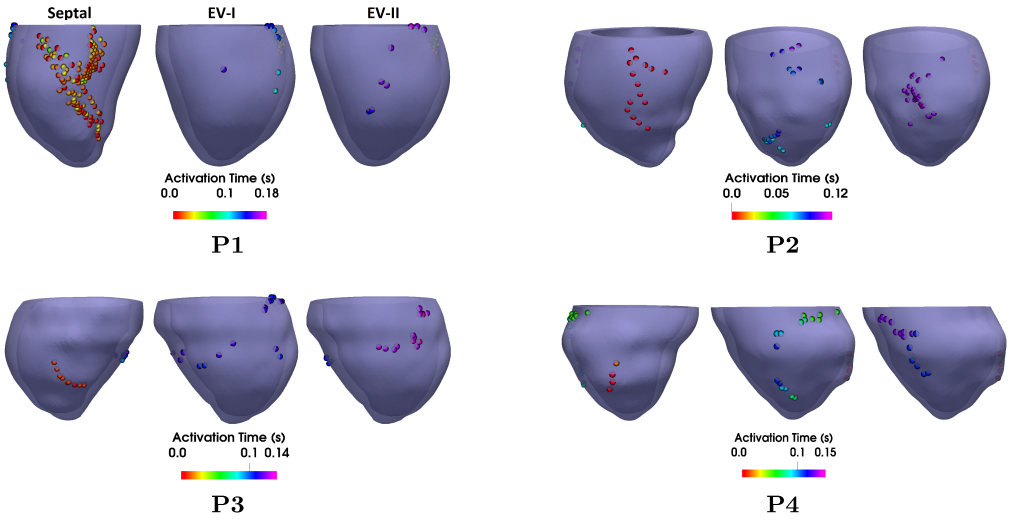

Figure 4: Maps of activation time after the alignment with the geometric MRI data. For each case: Left, septal data; Middle, epicardial veins data - group I (EV-I); Right, epicardial veins data - group II (EV-II).

3.3 Estimation of conductivities

We decided to use the septal measurements to define the applied current I_{app} in the Finite Elements approximation of problem (5), whereas the epicardial veins measurements were used to estimate the conductivities σ_f, σ_s and σ_n in (1) and to assess a significant step towards the validation in the context of a normal excitation of the monodomain model equipped with the Bueno-Orovio ionic model in a patient-specific context. Since in this work we considered patients without any scar, we assumed without loss of generality that the three conductivites are constant in space and time.

The applied current was built accordingly as follows:

$$I_{\text{app}}(\boldsymbol{x},t) = \begin{cases} 112500\ \mu A\ cm^{-3} & \text{if } (\boldsymbol{x},t) = (\boldsymbol{x}_j^S, \tau_j^S) \quad \text{for some } j = 1,\dots,N^S, \\ 0\ \mu A\ cm^{-3} & \text{elsewhere.} \end{cases}$$

The value of the applied current was chosen as the lowest value able to allow the electrical signal to propagate in the ventricle [40].

In what follows, we specified how the activation times τ_j^{h-I} and τ_j^{h-II} at the two groups of epicardial veins points were computed from the numerical simulations. In particular, τ_j^{h-I} (resp. τ_j^{h-II}) has been defined as the discrete time instant where the Finite Elements approximation of the trans-membrane potential u_h[1] at the computational point $\boldsymbol{x}_j^{V-I}$ (resp. $\boldsymbol{x}_j^{V-II}$) varies at its highest

[1]With a slight abuse of notation, we denote by u_h the Finite Elements time discretized solution u_h^n.

rate, *i.e.*

$$\tau_j^{h-\beta} = t^{\bar{n}}, \quad \text{where } \bar{n} = \arg\max_n \left| \frac{u_h^n\left(\boldsymbol{x}_j^{V-\beta}\right) - u_h^{n-1}\left(\boldsymbol{x}_j^{V-\beta}\right)}{\Delta t} \right| \quad \beta = I, II, \tag{7}$$

where a first order Euler approximation has been used, consistently with the order of the monodomain time discretization.

In order to maximize the agreement between numerical simulations and clinical measurements, we looked for the conductivities $\boldsymbol{\sigma} = (\sigma_f, \sigma_s, \sigma_n)$ in the physiological range $\Sigma = (0.70, 2.20) \times (0.16, 0.48) \times (0.03, 0.10))$ $k\Omega^{-1}cm^{-1}$ [23, 12, 11, 32, 19]. Specifically, we wanted to minimize the discrepancy between the computed activation times τ_j^{h-I} and the epicardial veins measures belonging to group I τ_j^{V-I}. To this aim, we introduced the following discrete functional:

$$F(u_h(\boldsymbol{\sigma})) = \sum_{j=1}^{N^{V-I}} \frac{1}{2} \left| \tau_j^{h-I}(u_h(\boldsymbol{\sigma})) - \tau_j^{V-I} \right|^2, \tag{8}$$

where $\widetilde{\boldsymbol{\sigma}}$ is a reference value of the conductivities used in the regularization term. Notice that we have highlighted the dependence of u_h on $\boldsymbol{\sigma}$.

The optimization problem then reads: Find the optimal value $\widehat{\boldsymbol{\sigma}}$ such that

$$\widehat{\boldsymbol{\sigma}} = \arg\min_{\boldsymbol{\sigma} \in \Sigma} F(u_h(\boldsymbol{\sigma})), \tag{9}$$

subjected to the Finite Elements approximation of the discretized-in-time monodomain problem (4)-(5)-(6).

To solve minimization problems similar to the previous one, some efficient strategies have been proposed for example in [15] for synthetic data and [1] for optical measurements on animal hearts. Here, since we considered a minimization problem with *in-vivo* human electrical data, we followed a basic *direct search* which is robust with respect to the noise of the electrical data. This is based on starting by an initial guess of $\boldsymbol{\sigma}$ taken in Σ and on ongoing corrections obtained by solving the monodomain problem and by evaluating the functional (8).

4 Numerical results

In this section, we show the numerical results obtained in terms of conductivities estimation and corresponding comparison between measured and computed activation times.

The Laplace-Dirichlet rule-based fiber generation algorithm described in [18], as well as all the numerical methods for the monodomain equation presented in Section 2, have been implemented within `life`$^{\mathtt{x}}$ (`(https://lifex.gitlab.io/lifex)`,

a new in-house developed high-performance `C++` library mainly focused on cardiac applications, based on the `deal.II` Finite Element core [9]; for further details on the implementation of the fibers generation see [36]. We have used Finite Elements of order 1, time step $\Delta t = 0.025ms$ [27, 31], characteristic mesh size $h \simeq 0.35mm$ [16] and a set of parameters for (2)-(3) reported in Table 2. Notice that both the values of Δt and h are small enough to allow the recovery of an accurate propagation front.

$\chi\ [F/m^2]$	$C_m\ [m^{-1}]$	$V_o\ [s]$	$V_1\ [s]$	$V_2\ [s]$	$\widetilde{V}\ [s]$	$\tau_1\ [s]$
0.01	1×10^5	0.006	0.3	0.015	1.58	11×10^{-3}

$\tau_3\ [s]$	$\tau_{o1}\ [s]$	$\tau_{o2}\ [s]$	$\tau_{21}\ [s]$	$\tau_{22}\ [s]$
2.8723×10^{-3}	6×10^{-3}	6×10^{-3}	43×10^{-3}	0.2×10^{-3}

Table 2: Values of the coefficients used in (5)-(6) [2].

In Table 3 we report the estimation of the conductivities obtained for the four patients by solving the minimization problem (9). Notice that all the values fall in the physiological range Σ reported in Section 3.3.

	$\widehat{\sigma}_f$	$\widehat{\sigma}_s$	$\widehat{\sigma}_n$
P1	1.11	0.21	0.05
P2	1.87	0.41	0.08
P3	1.23	0.25	0.07
P4	1.39	0.30	0.07

Table 3: Values of the optimal conductivity $\widehat{\boldsymbol{\sigma}}$ expressed in $k\Omega^{-1}cm^{-1}$.

In Figure 5 we show for the four patients the action potential at different instants computed by the numerical simulations with the estimated conductivities reported above.

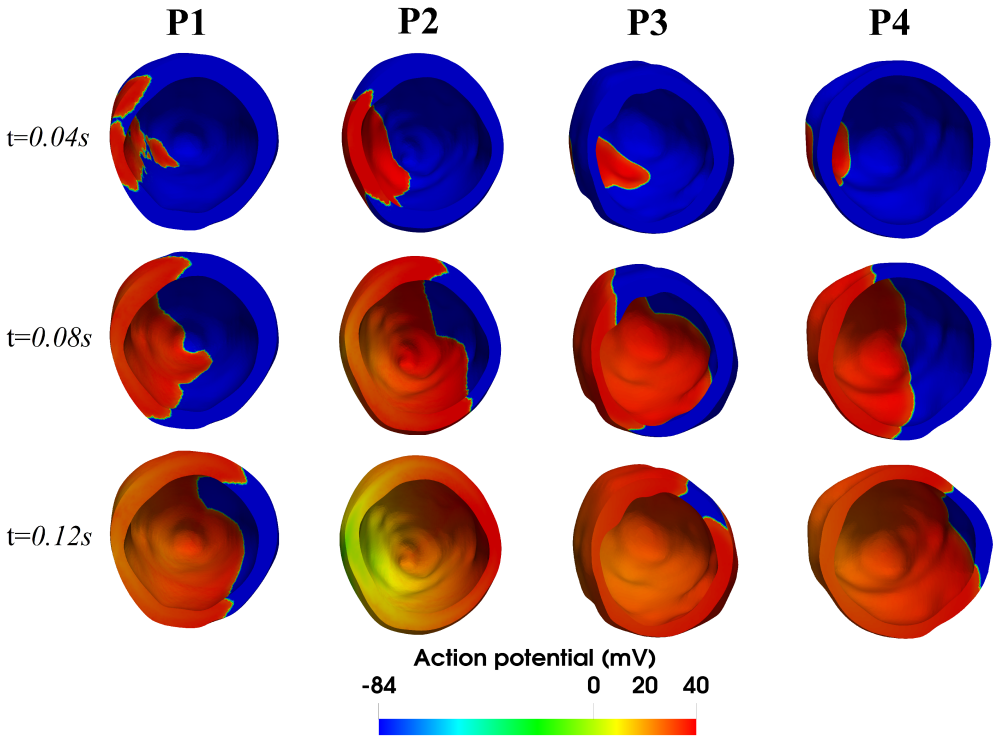

Figure 5: Action potential from the base view of the computational domain. In each row different time instants and in each column different patients are shown.

As highlighted by this figure, we have assumed that the region activated first is the septum, where measurements are available. This is in accordance with the fact that the patients suffer from LBBB, thus the signal does not enter the left ventricle through the Purkinje network as in the normal propagation [13, 37, 6], rather through the septum activated by the right ventricle.

According to (7), in Figure 6 we report the activation times corresponding to the previous numerical results (continuous map) together with the measurements (bullets).

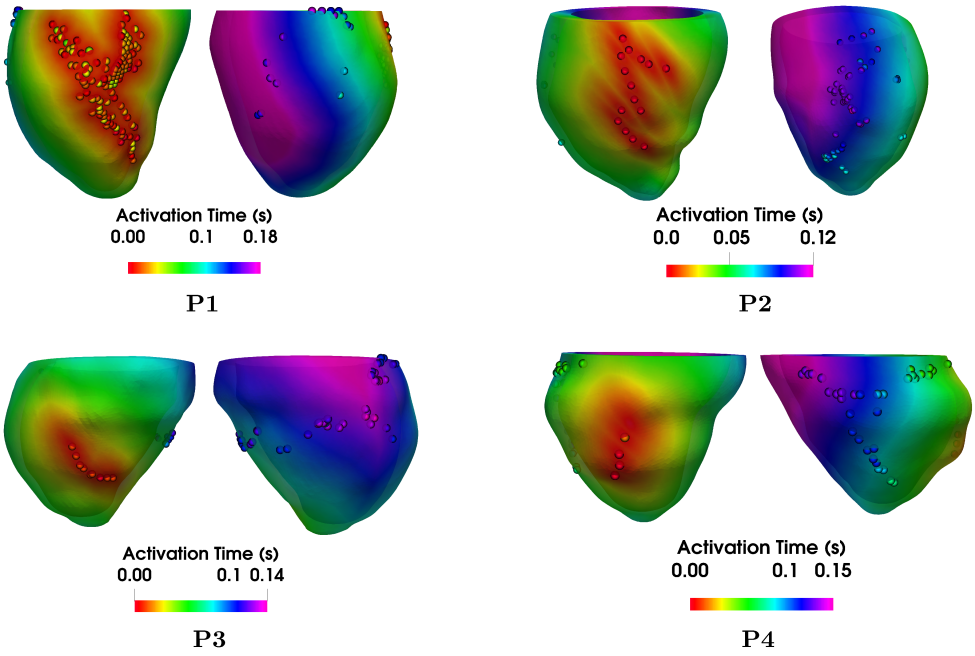

Figure 6: Computed activation times obtained by numerical solutions (continuous maps) and clinical measurements of activation times (bullets).

From these results, we observe an excellent qualitative agreement between the computed and measured activation times at the epicardial veins also for group II, that is those with highest values. We remember that the latter measurements were not used in the minimization problem, thus we have here provided a fair cross validation of the monodomain problem in the context of a normal excitation.

In order to go more in depth in the error analysis, in Table 4 we report the values of the errors computed for each patient. In particular, we computed the errors $e_j^{II} = |\tau_j^{V-II} - \tau_j^{h-II}|$ and the corresponding mean relative value $e^{II} = \dfrac{1}{N^{V-II}} \displaystyle\sum_j \frac{e_j^{II}}{\max_i \tau_i^{V-II}}$ and standard deviation over the total number of epicardial veins measurements belonging to group II, see Table 1.

Patient	Mean relative error e^{II} [%]	Standard deviation [%]
P1	6.17	3.28
P2	4.12	2.19
P3	5.05	2.88
P4	5.42	1.95

Table 4: Values of the mean relative errors, over the whole set of epicardial veins data belonging to group II, between numerical results and measurements and corresponding standard deviation.

For all the four cases, in Figure 7 we report the *boxplots* of the relative errors. This technique is useful to display groups of data through their quartiles. It is based on a five-number summary: the minimum and the maximum values of the dataset (shown by the lower and the upper lines on the whisker), the median (red dashed line), and the first and third quartile (lower and upper bounds of the box). To better show the distribution of the errors, we also reported the values of the single relative error by using green dots.

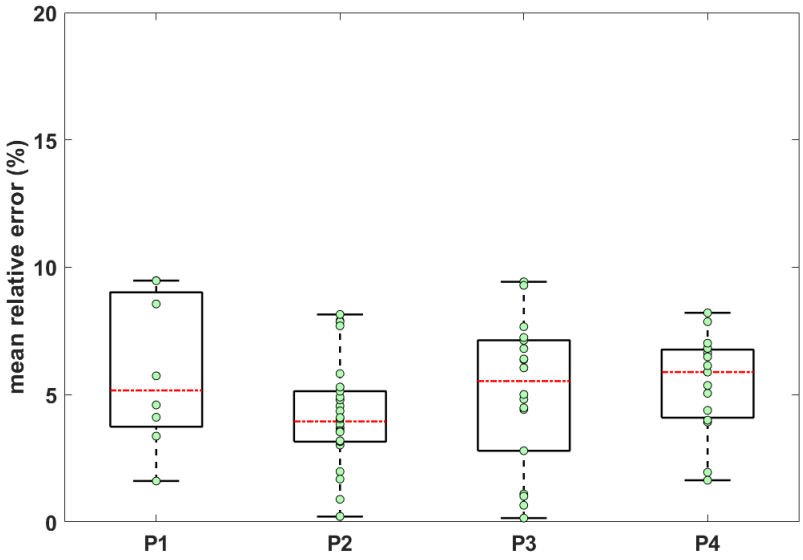

Figure 7: Boxplots of relative errors for the four patients with minimum and maximum values, median, and first and third quartiles.

From these results, we observe an excellent quantitative agreement between epicardial vein measurements not used in the parameter estimation (group II) and our computed results. The mean error was in any case below 6.2% and the standard deviation confirmed a low error variability. We notice from Table 1

that for P2 and especially for P3 and P4 our accurate results were found with few input data (septal measurements). This means that it is enough to have at disposal very few measurements of activation times where the signal starts in order to well predict the activation in the epicardial veins. Moreover, from the statistical analysis reported in Figure 7, we can observe that the errors are quite well confined in a small region, the maximum relative error being in any case less than 10%.

The previous findings are of utmost importance for clinical applications. For example, for the *Cardiac Resynchronization Therapy* (CRT) cardiologists often uses the point with the latest activation time (LAT) at the epicardial veins to locate the left electrode [14, 43] Then, thanks to our accurate numerical method, this information can be provided without a complete mapping of the epicardial veins. Indeed, only a few septal data to provide the input and a few epicardial veins data for the parameter estimation (group I) are needed. This will shorten the invasive procedure based on the insertion of catheters (up to a couple of hours) and reduce the exposition of the patient to radiations.

5 Conclusions

In this paper we have performed an important step towards the validation of the monodomain model in the context of a normal excitation with sinus rhythm by using in-vivo data of activation times acquired in four patients. For each case, we have used a set of measures at the epicardial veins to calibrate the three conductivities and another set of measures at the same location to compute the error with the numerical results and assess an important step toward the validation of the model. The mean error found in this cross-validation test was in any case less than 6.2%.

The results of the present work could have important clinical implications. For example, our validated computational tool could be used to estimate with good accuracy the point with latest activation time, commonly used during CRT to locate the left electrode, with a reduced mapping procedure with respect to the traditional case. This will allow to reduce the time of exposition of the patient to an invasive procedure and to radiations.

Acknowledgements

This project has received funding from the European Research Council (ERC) under the European Union's Horizon 2020 research and innovation programme (grant agreement No 740132, iHEART - An Integrated Heart Model for the simulation of the cardiac function, P.I. Prof. A. Quarteroni). CV has been partially supported also by the H2020-MSCA-ITN-2017, EU project 765374 "ROMSOC - Reduced Order Modelling, Simulation and Optimization of Coupled systems". AQ and CV have been partially supported also by the Italian research project

MIUR PRIN17 2017AXL54F "Modeling the heart across the scales: from cardiac cells to the whole organ".

References

[1] Barone A., Gizzi A., Fenton F., Filippi S., and Veneziani A. Experimental validation of a variational data assimilation procedure for estimating space-dependent cardiac conductivities. *Computer Methods in Applied Mechanics and Engineering*, 358:112615, 2020.

[2] Bueno-Orovio A., Cherry E.M., and Fenton F.H. Minimal model for human ventricular action potentials in tissue. *Journal of Theoretical Biology*, 253(3):544–560, 2008.

[3] Hodgkin A.L. and Huxley A.F. A quantitative description of membrane current and its application to conduction and excitation in nerve. *The Journal of Physiology*, 117(4):500–544, 1952.

[4] Muzikant A.L., Hsu E.W., Wolf P.D., and Henriquez C.S. Region specific modeling of cardiac muscle: Comparison of simulated and experimental potentials. *Annals of Biomedical Engineering*, 30(7):867–883, 2002.

[5] Eitel C., Hindricks G., Dagres N., Sommer P., and Piorkowski C. EnSite velocity^{TM} cardiac mapping system: a new platform for 3d mapping of cardiac arrhythmias. *Expert Review of Medical Devices*, 7(2):185–192, 2010.

[6] Vergara C., Lange M., Palamara S., Lassila T., Frangi A.F., and Quarteroni A. A coupled 3D-1D numerical monodomain solver for cardiac electrical activation in the myocardium with detailed Purkinje network. *J. Comput. Phys*, 308:218–238, 2016.

[7] Vergara C., Palamara S., Catanzariti D., Nobile F., Faggiano E., C. Pangrazzi, Centonze M., Maines M., Quarteroni A., and Vergara G. Patient-specific generation of the Purkinje network driven by clinical measurements of a normal propagation. *Med. Biol. Eng. Comput.*, 52(10):813–826, 2014.

[8] Augustin C.M., Crozier A., Neic A., Prassl A.J., Karabelas E., Ferreira da Silva T., Fernandes J.F., Campos F., Kuehne T., and Plank G. Patient-specific modeling of left ventricular electromechanics as a driver for haemodynamic analysis. *EP Europace*, 18(suppl_4):iv121–iv129, 2016.

[9] Arndt D., Bangerth W., Clevenger T.C., Davydov D., Fehling M., Garcia-Sanchez D., Harper G., Heister T., Heltai L., Kronbichler M., Kynch R.M., Maier M., Pelteret J.-P., Turcksin B., and Wells D. The `deal.II` library, version 9.1. *Journal of Numerical Mathematics*, 2019. accepted.

[10] Deng D., Arevalo H., Pashakhanloo F., Prakosa A., Ashikaga H., McVeigh E., Halperin H., and Trayanova N. Accuracy of prediction of infarct-related arrhythmic circuits from image-based models reconstructed from low and high resolution MRI. *Frontiers in Physiology*, 6, 2015.

[11] Roberts D.E. and Scher A.M. Effect of tissue anisotropy on extracellular potential fields in canine myocardium in situ. *Circulation Research*, 50(3):342–351, 1982.

[12] Roberts D.E., Hersh L.T., and Scher A.M. Influence of cardiac fiber orientation on wavefront voltage, conduction velocity, and tissue resistivity in the dog. *Circulation Research*, 44(5):701–712, 1979.

[13] Vigmond E.J. and Clements C. Construction of a computer model to investigate sawtooth effects in the Purkinje system. *IEEE Trans Biomed Eng*, 54(3):389–399, 2007.

[14] Zanon F., Baracca E., Pastore G., Fraccaro C., Roncon L., Aggio S., Noventa F., Mazza A., and Prinzen F. Determination of the longest intrapatient left ventricular electrical delay may predict acute hemodynamic improvement in patients after cardiac resynchronization therapy. *Circulation: Arrhythmia and Electrophysiology*, 7(3):377–383, 2014.

[15] Yang H. and Veneziani A. Efficient estimation of cardiac conductivities via POD-DEIM model order reduction. *Applied Numerical Mathematics*, 115:180–199, 2017.

[16] Arevalo H.J., Vadakkumpadan F., Guallar E., Jebb A., Malamas P., Wu K.C., and Trayanova N.A. Arrhythmia risk stratification of patients after myocardial infarction using personalized heart models. *Nature Communications*, 7(1), 2016.

[17] Relan J., Pop M., Delingette H., Wright G.A., Ayache N., and Sermesant M. Personalization of a cardiac electrophysiology model using optical mapping and MRI for prediction of changes with pacing. *IEEE Transactions on Biomedical Engineering*, 58(12):3339–3349, 2011.

[18] Bayer J.D., Blake R.C., Plank G., and Trayanova N.A. A novel rule-based algorithm for assigning myocardial fiber orientation to computational heart models. *Annals of Biomedical Engineering*, 40(10):2243–2254, 2012.

[19] Stinstra J.G., Hopenfeld B., and MacLeod R.S. On the passive cardiac conductivity. *Annals of Biomedical Engineering*, 33(12):1743–1751, 2005.

[20] Ten Tusscher K.H.W.J., Mourad A., Nash M.P., Clayton R.H., Bradley C.P., Paterson D.J., Hren R., Hayward M., Panfilov A.V., and Taggart P. Organization of ventricular fibrillation in the human heart: experiments and models. *Experimental Physiology*, 94(5):553–562, 2009.

[21] Andrews L. A template for the nearest neighbor problem. *C/C++ Users Journal*, 19(11):40–49, 2008.

[22] Antiga L., Piccinelli M., Botti L., Ene-Iordache B., Remuzzi A., and Steinman D.A. An image-based modeling framework for patient-specific computational hemodynamics. *Medical & Biological Engineering & Computing*, 46(11):1097–1112, 2008.

[23] Clerc L. Directional differences of impulse spread in trabecular muscle from mammalian heart. *The Journal of Physiology*, 255(2):335–346, 1976.

[24] Wang L., Dawoud F., Yeung S., Shi P., Wong K.C.L., Liu H., and Lardo A.C. Transmural imaging of ventricular action potentials and post-infarction scars in swine hearts. *IEEE Transactions on Medical Imaging*, 32(4):731–747, 2013.

[25] Fedele M. Polygonal surface processing and mesh generation tools for numerical simulations of the complete cardiac function. MOX Report 32, Politecnico di Milano, 2019.

[26] Potse M., Dube B., Richer J., Vinet A., and Gulrajani R.M. A comparison of monodomain and bidomain reaction-diffusion models for action potential propagation in the human heart. *IEEE Transactions on Biomedical Engineering*, 53(12):2425–2435, 2006.

[27] Fernández M.A. and Zemzemi N. Decoupled time-marching schemes in computational cardiac electrophysiology and ECG numerical simulation. *Mathematical Biosciences*, 226(1):58–75, 2010.

[28] German Cancer Research Center Division of Medical Image Computing. Medical imaging interaction toolkit. *http://www.mitk.org/wiki/MITK*, 2015.

[29] Colli Franzone P., Pavarino L.F., and Taccardi B. Simulating patterns of excitation, repolarization and action potential duration with cardiac bidomain and monodomain models. *Mathematical Biosciences*, 197(1):35–66, 2005.

[30] Colli Franzone P., Pavarino L.F., and Savaré G. Computational electrocardiology: mathematical and numerical modeling. In *Complex Systems in Biomedicine*, pages 187–241. Springer Milan, 2006.

[31] Colli Franzone P., Pavarino L.F., and Scacchi S. *Mathematical Cardiac Electrophysiology*. Springer International Publishing, 2014.

[32] Le Guyader P., Trelles F., and Savard P. Extracellular measurement of anisotropic bidomain myocardial conductivities. i. theoretical analysis. *Annals of Biomedical Engineering*, 29(10):862–877, 2001.

[33] Pathmanathan P., Bernabeu M.O., Niederer S., Gavaghan D.J., and Kay D. Computational modelling of cardiac electrophysiology: explanation of the variability of results from different numerical solvers. *International journal for numerical methods in biomedical engineering*, 28(8):890–903, 2012.

[34] A. Quarteroni, L. Dede', A. Manzoni, and C. Vergara. *Mathematical Modelling of the Human Cardiovascular System-Data, Numerical Approximation, Clinical Applications*. Cambridge University Press, 2019.

[35] Bordas R., Gillow K., Lou Q., Efimov I.R., Gavaghan D., Kohl P., Grau V., and Rodriguez B. Rabbit-specific ventricular model of cardiac electrophysiological function including specialized conduction system. *Progress in Biophysics and Molecular Biology*, 107(1):90–100, 2011.

[36] Piersanti R., Dede' L., Vergara C., Corno A.F., and Quarteroni A. Numerical methods for generating cardiac muscle fibersin ventricular and atrial electrophysiology simulation. *In preparation*.

[37] Bordas R.M., Gillow K., Gavaghan D., Rodríguez B., and Kay D. A Bidomain model of the ventricular specialized conduction system of the heart. *SIAM J. Appl. Math.*, 72(5):1618–1643, 2012.

[38] Krishnamoorthi S., Perotti L.E., Borgstrom N.P., Ajijola O.A., Frid A., Ponnaluri A.V., Weiss J.N., Qu Z., Klug W.S., Ennis D.B., and Garfinkel A. Simulation methods and validation criteria for modeling cardiac ventricular electrophysiology. *PLoS ONE*, 9(12):e114494, 2014.

[39] Krishnamoorthi S., Sarkar M., and Klug W.S. Numerical quadrature and operator splitting in finite element methods for cardiac electrophysiology. *International journal for numerical methods in biomedical engineering*, 29(11):1243–1266, 2013.

[40] Niederer S., Kerfoot E., Benson A.P., Bernabeu M.O., Bernus O., Bradley C., Cherry E.M., Clayton R., Fenton F., Garny A., Heidenreich E., Land S., Maleckar M., Pathmanathan P., Plank G., Rodrìguez J.F., Roy I., Sachse F.B., Seemann G., Skavhaug O., and Smith N.P. Verification of cardiac tissue electrophysiology simulators using an n -version benchmark. *Philosophical Transactions of the Royal Society A: Mathematical, Physical and Engineering Sciences*, 369(1954):4331–4351, 2011.

[41] Niederer S., Plank G., Chinchapatnam P., Ginks M., Lamata P., Rhode K.S., Rinaldi C.A., Razavi R., and Smith N.P. Length-dependent tension in the failing heart and the efficacy of cardiac resynchronization therapy. *Cardiovascular Research*, 89(2):336–343, 2010.

[42] Palamara S., Vergara C., Catanzariti D., Faggiano E., Pangrazzi C., Centonze M., Nobile F., Maines M., and Quarteroni A. Computational generation of the Purkinje network driven by clinical measurements: the

case of pathological propagations. *Int. J. Numer. Meth. Biomed. Engng.*, 30(12):1558–1577, 2014.

[43] Liang Y., Yu H., Zhou W., Xu G., Sun Y., Liu R., Wang Z., and Han Y. Left ventricular lead placement targeted at the latest activated site guided by electrophysiological mapping in coronary sinus branches improves response to cardiac resynchronization therapy. *Journal of Cardiovascular Electrophysiology*, 26(12):1333–1339, 2015.

[44] Saad Y. and Schultz M.H. Gmres: A generalized minimal residual algorithm for solving nonsymmetric linear systems. *SIAM Journal on scientific and statistical computing*, 7(3):856–869, 1986.

MOX Technical Reports, last issues

Dipartimento di Matematica
Politecnico di Milano, Via Bonardi 9 - 20133 Milano (Italy)

16/2020 Paolucci, R.; Mazzieri, I.; Piunno, G.; Smerzini, C.; Vanini, M.; Ozcebe, A.G.
Earthquake ground motion modelling of induced seismicity in the Groningen gas field

18/2020 Fumagalli, A.; Scotti, A.; Formaggia, L.
Performances of the mixed virtual element method on complex grids for underground flow

17/2020 Cerroni, D.; Formaggia, L.; Scotti, A.
A control problem approach to Coulomb's friction

15/2020 Fumagalli, I.; Fedele, M.; Vergara, C.; Dede', L.; Ippolito, S.; Nicolò, F.; Antona, C.; Scrofani,
An Image-based Computational Hemodynamics Study of the Systolic Anterior Motion of the Mitral Valve

13/2020 Pozzi S.; Domanin M.; Forzenigo L.; Votta E.; Zunino P.; Redaelli A.; Vergara C.
A data-driven surrogate model for fluid-structure interaction in carotid arteries with plaque

14/2020 Calissano, A.; Feragen, A; Vantini, S.
Populations of Unlabeled Networks: Graph Space Geometry and Geodesic Principal Components

11/2020 Antonietti, P.F.; Facciola', C.; Houston, P.; Mazzieri, I.; Pennes, G.; Verani, M.
High-order discontinuous Galerkin methods on polyhedral grids for geophysical applications: seismic wave propagation and fractured reservoir simulations

12/2020 Azzolin, L.; Dede', L.; Gerbi, A.; Quarteroni, A.
Effect of fibre orientation and bulk value on the electromechanical modelling of the human ventricles

09/2020 Rea, F.; Ieva, F.,; Pastorino, U.; Apolone, G.; Barni, S.; Merlino, L.; Franchi, M.; Corrao, G.
Number of lung resections performed and long-term mortality rates of patients after lung cancer surgery: evidence from an Italian investigation

08/2020 Antonietti, P. F.; Facciolà, C.; Verani, M.
Polytopic Discontinuous Galerkin methods for the numerical modelling of flow in porous media with networks of intersecting fractures